Aeroacoustic simulation of bluff bodies with protrusions at moderate Reynolds number

Kusano, Kazuya
Department of Mechanical Engineering, Kyushu University

https://hdl.handle.net/2324/7183338

出版情報：Physics of Fluids. 36 (2), pp.027146-1-027146-15, 2024-02-29. AIP Publishing
バージョン：

Aeroacoustic simulation of bluff bodies with protrusions at moderate Reynolds number

Kazuya Kusano (草野和也)
Department of Mechanical Engineering, Kyushu University, 744 Motooka, Nishi-ku, Fukuoka, 819-0395, Japan
E-mail address: kusano@mech.kyushu-u.ac.jp

Abstract

This paper presents an evaluation of passive control methods that employ surface protrusions to mitigate the aerodynamic sound generated from a cylinder wake flow. Building on previous designs optimized for low Reynolds numbers (Re = 150) through adjoint-based aeroacoustic shape optimization, this study investigated the performance under a moderate Reynolds number (Re = 67,000) condition typical of mechanical engineering applications using aeroacoustic simulations based on the lattice Boltzmann method (LBM). Three configurations of surface protrusions were tested, all of which were found to significantly reduce the mean drag by at least 45% compared with that of an unmodified circular cylinder. Designs featuring rear protrusions outperformed the conventional splitter plate in terms of the sound reduction performance, with symmetrical protrusions on both the front and rear surfaces achieving a tonal sound reduction of 13 dB. However, a specific protrusion design increased the low-frequency sound owing to the intensified large-scale flow separation. These findings highlight the effectiveness of rear protrusions in suppressing wake oscillations and dipole sound generation in the subcritical Reynolds number range. Moreover, the study revealed the need to tailor the front protrusion shape to the Reynolds number for performance optimization.

Keywords

Computational aeroacoustics, Lattice Boltzmann method, Adjoint method, Bluff body, Flow-induced sound, Shape optimization

1. Introduction

Bluff bodies generate aerodynamic noise, which is an increasing concern in applications such as rear-view mirrors of automobiles[1–3], pantographs of high-speed trains[4–6], and aircraft landing gears[7–9]. In the automotive industry, the shift toward electrification has made aerodynamic noise more noticeable. Therefore, the development of control strategies for aerodynamic noise has become a research hotspot. Similarly, the aerodynamic noise generated in railways, particularly in high-speed trains, is more apparent than other types of noise, such as rolling noise, with increasing train speeds. Advances in noise-reduction technologies for aircraft jet engines have also highlighted the significance of airframe noise, including that generated by the landing gear.

Numerous studies have contributed toward the development of innovative sound control methods. Comprehensive insights into these methods can be found in relevant review articles[10–12]. The present paper delves into recent advancements in the control methods employed for bluff body flows and flow-induced sounds.

Various actuators have been explored for active flow control of bluff bodies, with dielectric barrier discharge (DBD) plasma actuators emerging as promising candidates owing to their high efficiency, applicability, and rapid response[13,14]. Optimization techniques, such as the genetic algorithm (GA)[15,16] and deep reinforcement learning[17–19], have been used to enhance the actuation strategies. Despite the advances in active control methods, some challenges remain for practical application. Although these methods provide a high flow control performance, they require higher implementation costs than their passive counterparts.

Various passive methods have been proposed to suppress the aerodynamic sound of circular cylinders, which are representative bluff bodies. A popular example is the insertion of a splitter plate in the near-wake region of a cylinder[20]. The splitter plate disrupts the interaction between the shear layers separated from the top and bottom surfaces of the cylinder, thereby mitigating vortex shedding. A flexible splitter plate can offer a superior sound reduction performance than a rigid one[21]. Another notable method involves the symmetric and concentric placement of arc plates behind a circular cylinder[22,23]. These arc plates inject vorticities with opposite signs into the separated shear layers, aiding in the mitigation of vortex shedding and sound generation. Coating of porous materials around the cylinder has also been effective toward drag and sound reduction[24]. Porous materials can effectively relax the energy of the vortices in various modes[25]. In addition, the introduction of wavy shapes in the spanwise direction can help stabilize the near wake and reduce the aerodynamic sound by attenuating the spanwise coherence of the wake flow[26,27].

Many of the proposed flow control devices have relatively simple human-derived shapes. Optimization methods are expected to help create more efficient devices with intricate geometries. For instance, aeroacoustic shape optimization was performed using an unsteady adjoint method to mitigate the cylinder aeolian tone[28,29]. The optimization results revealed that appropriately shaped protrusions can suppress the aeolian tone while reducing the mean drag. However, the above study was limited to a low-Reynolds-number condition (Re = 150). The effectiveness of such protrusions at high Reynolds numbers, which are typically observed in mechanical engineering applications, remains unclear.

This study examined the effectiveness of optimized shapes with protrusions for flows with a moderate Reynolds number ($\mathrm{Re} = 6.7 \times 10^4$). Aeroacoustic simulations were conducted on a circular cylinder and three optimized shapes with protrusions using the lattice Boltzmann method (LBM). The LBM can simulate flow and acoustic fields simultaneously and accurately at low-Mach-number conditions. Therefore, the LBM is considered to be a promising alternative to conventional compressible Navier–Stokes solvers for direct aeroacoustic simulations of low-Mach-number flows[30]. This study evaluated the effects of the protrusions on the flow and acoustic fields around the cylinder using the simulation results.

The remainder of this paper is organized as follows. Section 2 describes the shapes of the cylinder employed in this study. Section 3 outlines the numerical methods and computational conditions for the aeroacoustic simulations. Section 4 presents the simulation results. Finally, the main findings are summarized in Section 5.

2. Flow conditions and cylinder shapes

In the numerical study, the aerodynamic sound generated from the flow around a cylinder was considered. A circular cylinder with a diameter D served as the baseline, to which several passive control methods were applied. The Reynolds number can be defined as $\mathrm{Re} = U_\infty D/\nu$, where U_∞ is the free-stream velocity and ν is the dynamic viscosity.

In a previous study[29], shape optimization was conducted at a Reynolds number (Re) of 150 using 2D simulations, resulting in three optimized shapes, as shown in Fig. 1 (a)-(c). Figure 1 (a) and (b) show the optimized shapes of the rear and front surfaces, respectively. The shapes were constrained to be symmetrical with respect to the streamwise direction. The shape depicted in Fig. 1 (c) results from the optimization of both surfaces while ensuring symmetry in the streamwise and vertical directions. These optimized shapes are characterized by protrusions on the front, rear, or both surfaces. It seems likely that the front protrusions evolved to anchor the separation points to their tips, whereas the rear protrusions evolved to disrupt the interaction between the top and bottom shear layers. The study demonstrated that these protrusions are effective in reducing the aeolian tone and mean drag at $\mathrm{Re} = 150$.

However, it is unclear whether these shapes are effective for engineering applications at high Reynolds numbers. Conducting optimizations at high Reynolds numbers using 3D simulations can be computationally expensive. Therefore, shapes optimized for low-Reynolds-number flows were employed for high-Reynolds-number flows in this study. Changes in the flow and acoustic fields relative to an unmodified circular shape were investigated using direct aeroacoustic simulations.

The free-stream velocity was 50 m/s, and the corresponding Mach number was 0.146. The diameter of the circular cylinder was 20 mm, resulting in a Reynolds number of 6.7×10^4. As shown in Fig. 1 (a)-(c), the streamwise length of the cylinder increased in the modified shapes, indicating that the actual Reynolds number also increased for controlled cases. For the cylinder with protrusions on both the front and rear surfaces, the streamwise length increased to 1.84*D*, resulting in a Reynolds number of 1.2×10^5 based on this length, which is still within the subcritical range.

For comparison with the conventional passive control method, a circular cylinder with an attached splitter plate, as shown in Fig. 1 (d), was evaluated. The splitter had a length of 0.5*D* and a width of 0.02*D*.

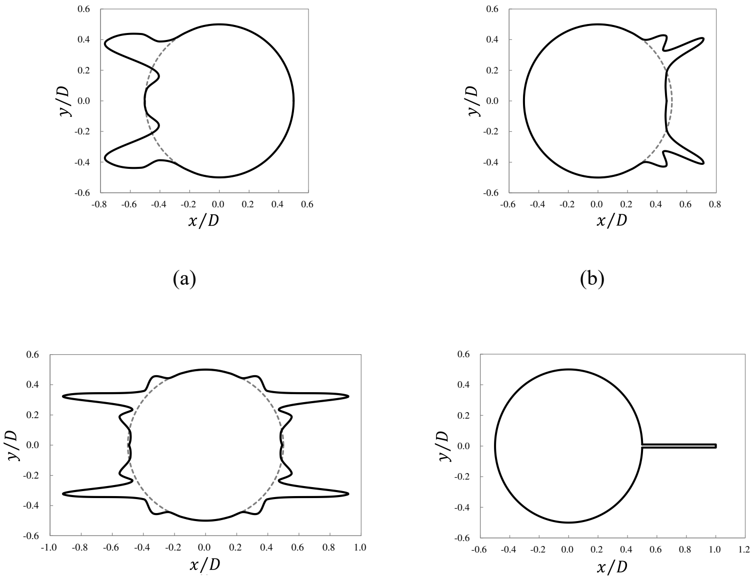

(a) (b)

(c) (d)

Fig. 1. Passive flow control methods for cylinders: (a) Front protrusions, (b) rear protrusions, (c) front and rear symmetric protrusions, and (d) splitter plate.

3. Numerical method

3.1. Lattice Boltzmann method

The flow and acoustic fields around the cylinder were simultaneously simulated using the LBM. The LBM can simulate the behavior of fluids that are weakly compressible under low-Mach-number conditions. It computes the particle motions, including streaming and collision processes, using a regular grid. Within the grid, the particle velocity is discretized into a finite number of velocities. In this study, a 3D model with twenty-seven discrete velocities (D3Q27) arranged along a cubic lattice was employed, as shown in Fig. 1. The particle velocities $\mathbf{c}_i = \left[|c_{ix}\rangle, |c_{iy}\rangle, |c_{iz}\rangle\right]$ of the D3Q27 model can be defined as follows:

$$\begin{aligned} |c_{ix}\rangle &= [0, c, -c, 0,0,0,0, c, -c, c, -c, c, -c, c, -c, 0,0,0,0, c, -c, c, -c, c, -c, c, -c]^{\mathrm{T}}, \\ |c_{iy}\rangle &= [0,0,0, c, -c, 0,0, c, c, -c, -c, 0,0,0,0, c, -c, c, -c, c, c, -c, -c, c, c, -c, -c]^{\mathrm{T}}, \\ |c_{iz}\rangle &= [0,0,0,0,0, c, -c, 0,0,0,0, c, c, -c, -c, c, c, -c, -c, c, c, c, c, -c, -c, -c, -c]^{\mathrm{T}}, \end{aligned} \tag{1}$$

where $|\cdot\rangle$ denotes a 27-dimensional column vector, and $c = \Delta x / \Delta t$ represents the particle speed. Here, Δx and Δt denote the grid spacing and time increment, respectively.

The distribution function of a particle with velocity $\mathbf{c}_i$ at position **x** and time *t* is represented by $f_i(t, \mathbf{x})$. This function evolves over time based on the lattice Boltzmann equation (LBE). In this study, the cascaded collision operator[31,32] was employed to facilitate stable simulations of high-Reynolds-number flows. The LBE with the cascaded collision operator is expressed as follows:

$$|f_i(t + \Delta t, \mathbf{x} + \Delta t \mathbf{c}_i)\rangle = |f_i(t, \mathbf{x})\rangle - \mathbf{M}^{-1}\mathbf{N}^{-1}\mathbf{S}\left[|\widetilde{T}_i(t, \mathbf{x})\rangle - |\widetilde{T}_i^{\,\mathrm{eq}}(t, \mathbf{x})\rangle\right], \tag{2}$$

where $|\widetilde{T}_i\rangle = \mathbf{NM}|f_i\rangle$ represents the central moments, and $|\widetilde{T}_i^{\,\mathrm{eq}}\rangle$ denotes the equilibrium central moments. $\mathbf{M}$ is a transformation matrix that converts the distribution functions into raw moments, and $\mathbf{N}$ is a shift matrix that transforms the raw moments into central moments. Specific values of $\mathbf{M}$ and $\mathbf{N}$ can be found elsewhere[32]. The right side of Eq. (2) suggests that the particle relaxation toward the equilibrium state is calculated within the central moment space. $\mathbf{S}$ is a diagonal relaxation matrix, defined as follows:

$$\begin{aligned} \mathbf{S} = \mathrm{diag}\Bigg\{ & s_0, s_1, s_1, s_1, s_v, s_v, s_v, \begin{bmatrix} s_+ & s_- & s_- \\ s_- & s_+ & s_- \\ s_- & s_- & s_+ \end{bmatrix}, s_3, s_3, s_3, s_3, s_3, s_3, \\ & \begin{bmatrix} s_+ & s_- & s_- \\ s_- & s_+ & s_- \\ s_- & s_- & s_+ \end{bmatrix} s_{3b}, s_4, s_4, s_4, s_{4b}, s_{4b}, s_{4b}, s_5, s_5, s_5, s_6 \Bigg\}, \end{aligned} \tag{3}$$

where $s_+ = (s_{2b} + 2s_2)/3$, and $s_- = (s_{2b} - 2s_2)/3$. The relaxation parameter s_2 is determined based on the relationship with the kinematic viscosity ν of the fluid, as follows:

$$s_2 = \left(\frac{1}{2} + \frac{3\nu}{\Delta t c^2}\right)^{-1}. \tag{4}$$

In this study, ν encompassed the molecular and eddy viscosities, with the latter being calculated using the WALE model[33,34]. The other free parameters in $\mathbf{S}$ were set to 1.0.

The equilibrium central moments $|\widetilde{T}_\iota^{\mathrm{eq}}\rangle$ are defined as follows:

$$|\widetilde{T}_\iota^{\mathrm{eq}}\rangle = [\rho, 0,0,0,0,0,0, \rho c_s^2, \rho c_s^2, \rho c_s^2, 0,0,0,0,0,0,0, \rho c_s^4, \rho c_s^4, \rho c_s^4, 0,0,0,0,0,0, \rho c_s^6]^{\mathrm{T}}. \tag{5}$$

where ρ is the fluid density, and $c_s = c/\sqrt{3}$ is the speed of sound.

The fluid density ρ and velocity $\mathbf{u}$ are obtained by calculating the particle velocity moments of the distribution functions as follows:

$$\rho = \sum_i f_i\,, \qquad \rho\mathbf{u} = \sum_i f_i \mathbf{c}_i. \tag{6}$$

The fluid pressure is related to the density as $p = \rho c_s^2$. Given that low-Mach-number flows have negligible temperature variation, utilizing the athermal approximation in aeroacoustic simulations is considered reasonable.

3.2. Computational domain and grids

The computational domain measured 1024*D*, 1024*D*, and 8*D* in the streamwise (*x*), crossflow (*y*), and spanwise (*z*) directions, respectively. The spanwise correlation length of a circular cylinder at $\mathrm{Re} = 6.7 \times 10^4$ is known to be approximately 2-3*D*[35]. The domain can include several flow structures in the spanwise direction. The origin was set at the center of the mid-span cross-section of the cylinder. Figure 2 shows the computational domain and outlines of the computational grid. The cylinder was positioned centrally within this domain. As shown in the figure, a hierarchically refined Cartesian grid based on the building-cube method[36] was used to discretize the computational domain. Although the cascaded model enhances the stability in computations compared with the standard Bhatnagar–Gross–Krook (BKG) model, numerical instabilities can be observed in coarser sections when such grids are used. To mitigate these numerical instabilities, a sixth-order implicit filtering scheme[37] was applied to the distribution function at each time step.

The maximum grid spacing was 0.5*D*. The points per wavelength (PPW) for the aeolian tone were estimated to be 69, which is sufficiently high to accurately resolve the propagation of sound waves of high-frequency sounds up to approximately a quarter of the tonal sound. As shown in Fig. 2 (b), the finest and second-finest grids were arranged around the cylinder and wake regions. For the circular cylinder, the three minimum spacings listed in Table 1 were used to evaluate the sensitivity of the grid resolution near the cylinder. The finest grid was used for the other shapes. In the finest grid, the minimum grid spacing was $3.9 \times 10^{-3} D$, and the total number of grid points was approximately 1.5 billion.

3.3. Boundary conditions

The free-stream density and velocity were specified using local equilibrium functions at the outer boundaries in the streamwise and crossflow directions, respectively. Periodic boundary conditions were employed in the spanwise direction. Moreover, an absorbing treatment[38] was implemented for $r > 256C$ to prevent sound waves from reflecting on the outer boundaries of the domain, where r is the radial coordinate, defined as $r = x^2 + y^2$. In this region, the distribution functions were forced to gradually decay along the radial direction to the local equilibrium function calculated based on the free-stream density and velocity.

The boundary conditions on the cylinder surface were determined using the interpolated bounce-back (IBB) scheme. This scheme allows the consideration of wall boundaries located between the grid points by interpolating the distribution function on the boundaries based on the bounce-back rule. The linear interpolation scheme proposed by Bouzidi et al. [39] was employed in this study. This scheme is expressed as follows:

$$\hat{f}_{\bar{\imath}}(t+\Delta t, \mathbf{x}_b) = \begin{cases} 2q_i \hat{f}_i(t, \mathbf{x}_b) + (1-2q_i)\hat{f}_i(t, \mathbf{x}_b - \Delta t \mathbf{c}_i) & (q_i < 1/2) \\ \dfrac{1}{2q_i}\hat{f}_i(t, \mathbf{x}_b) + \dfrac{(2q_i - 1)}{2q_i}\hat{f}_{\bar{\imath}}(t, \mathbf{x}_b) & (q_i \geq 1/2) \end{cases}, \tag{7}$$

where $\bar{\imath}$ denotes the direction opposite to i, and $\hat{f}$ denotes the distribution function after the collision operation; $\mathbf{x}_b$ is the closest node to the wall in the fluid, and q_i represents the distance between the node $\mathbf{x}_b$ and the wall ($0 \leq q_i < \Delta x$). Equation (7) provides the wall boundary condition by linear interpolation, using the distribution functions at $\mathbf{x}_b$ and its adjacent node $\mathbf{x}_b - \mathbf{c}_i \Delta t$.

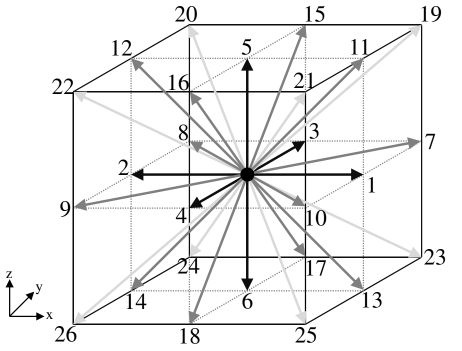

Fig. 2. D3Q27 model used for the numerical simulation.

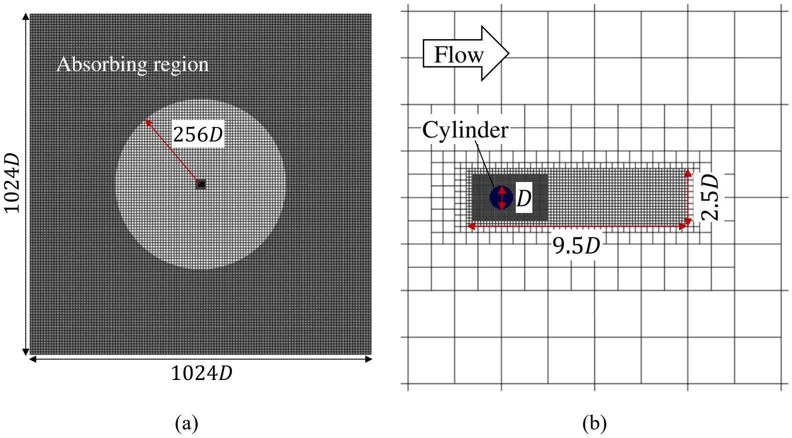

Fig. 3. Computational domain and grid: (a) Overall view, and (b) close-up view around the cylinder.

Table 1. Information on computational grids.

	Minimum grid spacing	**Maximum grid spacing**	**Grid size [billion]**
Coarse	$1.6 \times 10^{-2}D$	$0.5D$	0.16
Medium	$7.8 \times 10^{-3}D$	$0.5D$	0.57
Fine	$3.9 \times 10^{-3}D$	$0.5D$	1.50

4. **Results and discussion**

4.1. **Validation of simulation results**

The simulation results of the present study for a circular cylinder were validated by comparing them with the results of other numerical and experimental studies[40–43]. Table 2 presents the drag coefficient, lift coefficient, and Strouhal number calculated using the LBM and those obtained from the literature[40–43]. The LBM using the coarse grid underestimated the mean drag and RMS of the drag and lift fluctuations compared with the results in existing studies. These values increased and converged with grid refinement. As shown in the table, the LBM results obtained using the fine grid are consistent with the results in the literature.

The distributions of the pressure coefficient C_p on the cylinder surface obtained from the LBM simulations were compared with those obtained from an experiment[44], as shown in Fig. 4. In the figure, the azimuth angle θ is defined such that $\theta = 180°$ coincides with the streamwise direction. The distributions of the time-averaged pressure coefficients (Fig. 4 (a)) revealed that the pressure reduction in the rear part of the cylinder was insufficient in the simulation when using the coarse grid. This resulted in the underestimation of the mean drag, as presented in Table 2. This discrepancy was alleviated in the simulation results of the medium and fine grids, with the latter aligning well with the experimental results.

Figure. 4 (b) shows the RMS of the fluctuations in the pressure coefficient on the cylinder surface. Clearly, the pressure fluctuations can be better simulated with increasing grid resolution. The peak pressure fluctuation in the simulation results of the fine and medium grids near $\theta = 80°$ corresponds to the time-averaged separation point, which appears slightly delayed compared with experimental results. The simulation results show a slight underestimation of the pressure drop around $\theta = 70°$ as shown in Fig. 4 (a), leading to a weaker pressure gradient in the streamwise direction than that observed experimentally. This could be a factor in the flow separation delay and can be attributed to the use of the Cartesian grid in the simulations. Additionally, the experimental data in Fig. 4 (b) indicate non-zero pressure fluctuations near $\theta = 0°$, indicating possible influence of freestream turbulence. Because the behavior of the separated shear layer is significantly affected by freestream turbulence, it can also contribute to the differences between simulation and experimental results at $\theta > 80°$. However, the simulation using the fine grid can effectively reproduce the experimental trends.

To validate the simulation results for the aerodynamic sound, Fig. 5 presents the power spectral densities (PSDs) of the sound pressure observed in the far field. The observation position was located $50D$ away from the cylinder in the crossflow direction. This figure shows a comparison of the simulation and experimental results[45]. The simulation and experiment were conducted under identical conditions, with $D = 20$ mm and $U_\infty = 50$ m/s. However, there was a difference between the cylinder span length in the simulation and experiment. In the experiment, the span length was $50D$, whereas in the simulations, it was considered infinite because of the application of periodic boundary conditions. Consequently, the computed sound pressure levels (SPLs) were corrected for the span length as follows[46]:

$$\mathrm{SPL}_c = \mathrm{SPL}_\infty + 10\log_{10}\left(\frac{L}{\pi R}\right), \tag{9}$$

where SPL_∞ is the SPL computed under the condition of an infinite span length, and SPL_c is the SPL corrected for the span length L in the experiment.

Figure 5 shows that the simulation using the coarse grid significantly underestimated the highest peak near St = 0.2. In comparison, the LBM using the medium and fine grids successfully simulated the total sound. Further, smaller turbulent eddies were captured with increasing grid resolution, thereby improving the sound prediction in the high-frequency range. The overall sound pressure level (OASPL) discrepancies between the coarse and medium grids compared with that of the fine grid were -13.0 dB and -0.7 dB, respectively. The minor difference between the fine and medium grids indicates good convergence of the grid resolution for the sound prediction. Based on these results, the fine grid was used to evaluate the passive control methods in subsequent sections.

Table 2. Comparison of the drag and lift coefficients and Strouhal number for various methods.

	Method	$\mathbf{Re/10^4}$	C_{D_mean}	C'_{D_rms}	C'_{L_rms}	$\mathrm{S_t}$
Present	LBM (coarse)	6.7	1.00	0.0197	0.132	0.20
	LBM (medium)		1.22	0.0513	0.497	0.20
	LBM (fine)		1.26	0.0828	0.556	0.19
Seo & Moon[40]	LES	4.3	1.24	0.1	0.54	0.187
Lloyd & James[41]	LES	6.3	1.27	-	0.63	0.189
Lesage & Gartshore[42]	Exp.	6.5	1.19	-	0.45	0.195
Zheng et al.[43]	Exp.	7.4	1.21	-	0.53	-

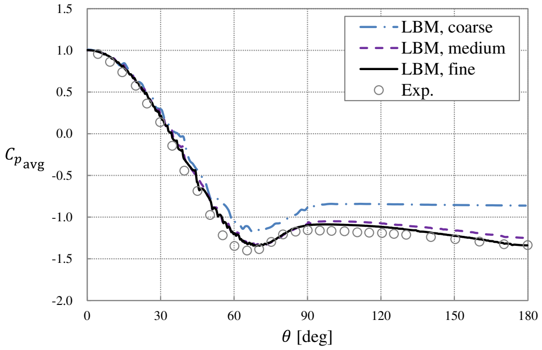

(a)

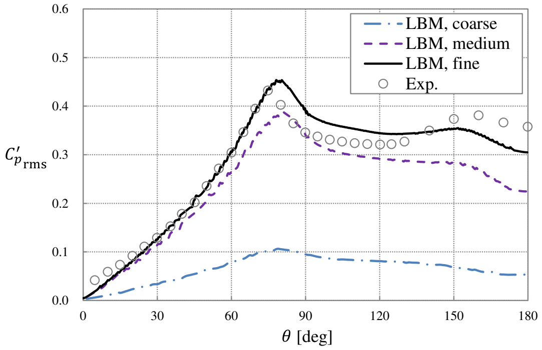

(b)

Fig. 4. Pressure coefficient distribution on a circular cylinder: (a) Time-averaged, and (b) RMS. The Reynolds number was $\mathrm{Re} = 6.7 \times 10^4$ in the present simulations and $\mathrm{Re} = 6.1 \times 10^4$ in the experiment, which was conducted by Nishimura and Taniike[44].

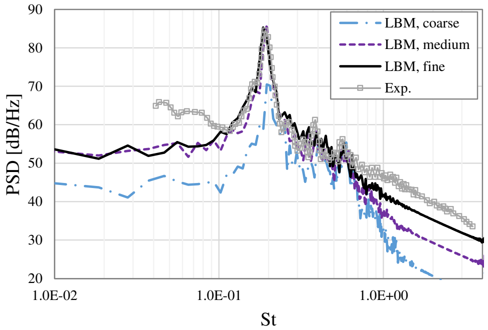

Fig. 5. PSDs of the sound pressure at $x/D = 0$, $y/D = 50$, and $z/D = 0$. The experimental results were reported by Xing et al[45].

4.2. **Protrusion effects on fluid forces and aerodynamic sounds**

Figure 6 shows a comparison of the time-averaged drag coefficients between the circular cylinder and the control devices. The mean drag of the circular cylinder without any control measure was $C_{D_{\text{mean}}} = 1.26$. All the passive control devices achieved a mean drag reduction of at least 45% compared with that of the uncontrolled cylinder. These data suggest that rear protrusions are more effective at drag reduction than front protrusions. Furthermore, the protrusions installed only on the rear surface exhibited a drag reduction comparable to that achieved with the splitter plate. The most significant reduction in the mean drag was observed when the protrusions were installed on both the front and rear surfaces, resulting in a decreased mean drag coefficient of $C_{D_{\text{mean}}} = 0.15$.

To examine the fluctuations in the fluid forces, the PSDs of the lift and drag coefficients were compared for cases with and without the use of any control methods, as shown in Fig. 7. A comparison of Fig. 7 (a) and (b) shows that the lift fluctuation is significantly higher than the drag fluctuation for all the cases. This lift fluctuation may have primarily contributed to the generation of aerodynamic sounds. Further, the PSDs of the lift coefficient indicate that the highest peak at a Strouhal number (St) of 0.19, observed for the unmodified circular cylinder, was altered by using the control methods. The splitter plate reduced the peak fluctuation without altering the peak frequency. The installation of protrusions on the rear surface alone or on both surfaces attenuated the peak fluctuations and shifted the peak frequency to higher values. Conversely, protrusions on the front surface alone increased the peak fluctuation and decreased the peak frequency. Among the control methods tested, installing protrusions on both surfaces proved to be the most effective in reducing the fluctuations in the lift. Moreover, Fig. 7 (b) shows that the drag fluctuation also was reduced, except for the front protrusion case. The peak frequency of the drag fluctuation corresponded to twice that of the lift fluctuation frequency in each case.

Figure 8 shows the PSDs of the sound pressures observed at $x/D = 0$, $y/D = 50$, and $z/D = 0$. The obtained sound spectra correlate with the lift fluctuation spectra shown in Fig. 7, except in the high-frequency range, which may have been due to contributed by wake turbulence. As shown in Fig. 8, the thin protrusions did not generate additional tonal sounds in the high-frequency range. Although the protrusions installed on the front surface decreased the aeolian tone at Re = 150, as demonstrated in a previous study[29], this modification increased the tonal sound at Re = 67,000. In comparison, the installation of protrusions on the rear surface alone, or on both surfaces decreased the tonal sound and proved to be more effective than the conventional splitter plate. The latter configuration resulted in a reduction in the peak level by approximately 13 dB. Among other passive control methods, porous coating is one of the methods that have received the most attention. A previous study[47] showed that the tonal sound can be reduced by up to 14 dB at Re = 6.3×10^4 by coating porous materials around a cylinder. These findings suggest that protrusions can achieve tonal sound reduction effects that are comparable to those of porous coating.

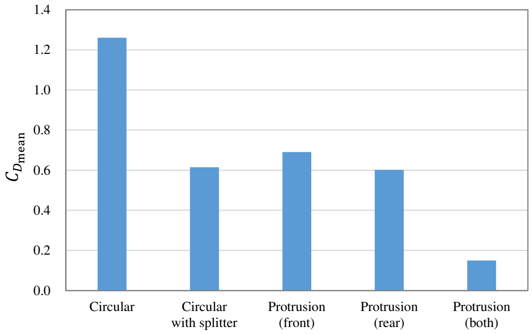

Fig. 6. Comparison of the mean drag coefficient between the circular cylinder and control methods.

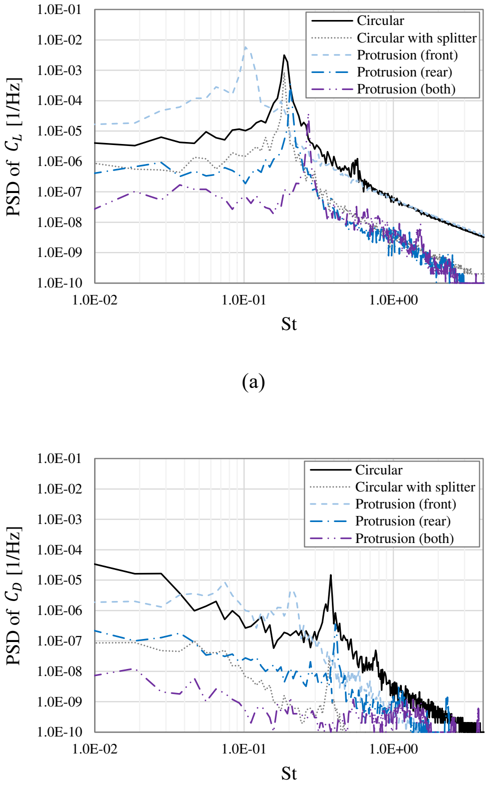

(a)

(b)

Fig. 7. Comparison of the PSDs of the (a) lift and (b) drag coefficients with and without control methods.

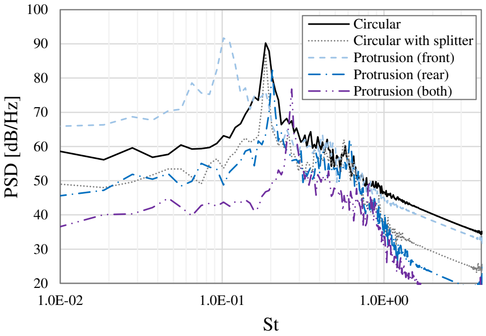

Fig. 8. Comparison of PSDs of the sound pressure at $x/D = 0$, $y/D = 50$, and $z/D = 0$ with and without control methods.

4.3. **Protrusion effects on flow field**

The effects of the control methods on the flow field around the cylinder are discussed in this section. Figure 9 shows the time- and spanwise-averaged pressure contours around the cylinder. In the case without control (Fig. 9 (a)), a notable pressure drop can be observed behind the cylinder, suggesting strong vortex shedding from the uncontrolled cylinder. Figure 9 (b)-(e) show that all the control methods involving protrusions can mitigate the pressure drop behind the cylinder. Notably, in the configuration with protrusions on both surfaces, the pressure in the cylinder wake approached that of the free stream, which correlates with the significant reduction in the mean drag shown in Fig. 6. For the uncontrolled case, the pressure coefficient at the rear stagnation point was -1.34. In contrast, this value increased to -0.23 for the configuration with protrusions on both surfaces. Moreover, Fig. 9 (b) and (d) show that there is a substantial pressure difference between the inside and outside of the front protrusions. Therefore, material strength and applicable flow velocity should be carefully considered for the front protrusion.

Figure 10 shows the time- and spanwise-averaged streamwise velocity contours and streamlines around the cylinder. Installing protrusions on the front surface changed the separation point to the protrusion tips, as shown in Fig. 10 (b) and (d). As shown in the Fig. 10 (b), the separated flow at the protrusion tips did not reattach to the cylinder surface, whereas in Fig. 10 (d), it did reattach. This difference may be attributed to the angle of the front protrusions with respect to the free-stream direction, which was optimized for Re = 150. These findings suggest that the shapes of the front protrusions should be tailored to specific Reynolds numbers. Figure 10 (a), (d), and (e) show that the wake of the cylinder with protrusions on both surfaces is substantially narrower than that of the uncontrolled cylinder and the cylinder with a splitter plate.

The changes in the wake width shown in Fig. 10 corresponded to the changes in the peak Strouhal number shown in Fig. 7 and 8. Specifically, a narrower wake width resulted in a higher peak Strouhal number. The figures also indicate that wake diffusion in the controlled cases was delayed compared with that in the uncontrolled case, implying that flow oscillation either occurred further downstream or was suppressed. Furthermore, Fig. 10 (b) and (d) show that the region between the front protrusions has streamlines passing through it and is not completely stagnated. This implies that this region cannot be filled with a solid.

Figure 11 shows the time-averaged streamwise velocity profiles along the y-axis for cases with and without the use of control methods, including a comparison between the current simulation results at Re = 67,000 and those of a previous study[29] at Re = 150, where shape optimizations were performed. The data indicate that the flow over the circular cylinder accelerated owing to a favorable pressure gradient, resulting in streamwise velocities near the cylinder that exceeded the free-stream velocity. No significant changes in the velocity profiles were observed for the cylinder with rear protrusions compared with the uncontrolled circular cylinder at either Reynolds number. While the front protrusions effectively moderated the velocity gradient around the cylinder at Re = 150, they led to a massive flow separation at Re = 67,000. In contrast, the protrusions on both surfaces successfully moderated the velocity gradient around the cylinder, even at Re = 67,000, potentially mitigating vortex shedding.

Figure 12 shows the instantaneous isosurfaces of the Q-criterion, colored by the spanwise vorticity, when the lift coefficient reaches its maximum. As shown in Fig. 12 (a), the laminar-separated shear layers transition to a turbulent flow, with a cluster of vortices exhibiting large oscillations in the crossflow direction within the wake. Figure 12 (b) and (d) demonstrate that the front protrusions caused flow separation, and the onset of turbulence transition occurred further upstream. Figure 12 (c) and (d) suggest that the rear protrusions disrupt the interactions between the upper and lower shear layers, resulting in a delayed wake oscillation compared with that in the uncontrolled case. The protrusions on both surfaces markedly suppressed flow oscillations compared with the uncontrolled cylinder and the cylinder with a splitter plate.

Figure 13 shows the instantaneous spanwise vorticity contours at the cross-section for $z/D = 0$ when the lift coefficient reaches its maximum. As shown in Fig. 13 (a), clusters of vortices are alternately formed from the top and bottom separated shear layers near the cylinder, exhibiting oscillations in the crossflow direction. With front protrusions, the cluster of vortices appears to be larger than that in the uncontrolled cylinder, as shown in Fig. 13 (b). This may have resulted from the pronounced large separation induced by the protrusions. Figure 13 (c) demonstrates that the rear protrusions delayed the development of the vortex cluster further downstream compared with the uncontrolled case and mitigated vertical oscillation of the vortices, similar to the effects of a splitter plate shown in Fig. 13 (e). Figure 13 (d) shows that the symmetrical protrusions on both surfaces notably inhibited both the formation of vortex clusters and the higher amplitudes of the wake oscillations.

Figure 14 shows the instantaneous cross-flow velocity contours at the cross-section for $y/D = 0$ when the lift coefficient reaches its maximum. These results show that all the control method yielded more delayed wake oscillations. Furthermore, the protrusions on both surfaces significantly alleviated the wake oscillation, as shown in Fig. 14 (d). As shown in Fig. 14 (a), the length of the spanwise coherent structures near $x/D = 1.0$ for the uncontrolled cylinder appears to be approximately $3D$, which is consistent with previous findings[35]. Figure 14 (e) suggests that the splitter plate may have decreased the spanwise coherent length in the near wake.

Figure 15 shows a comparison between the RMS values of the pressure fluctuations in the near-field region. In the uncontrolled cylinder, the pressure fluctuations were highest immediately behind the cylinder. These pressure fluctuations originated from vigorous vortex shedding, as shown in Fig. 13 (a). The application of the four control methods resulted in lower pressure fluctuations behind the cylinder compared with that of the uncontrolled case, as shown in Fig. 15 (b)-(e). In particular, Fig. 15 (c) and (d) indicate that pressure fluctuations were significantly suppressed between the rear protrusions owing to the reduced oscillation in the shear layers. Moreover, the peaks in the pressure fluctuations shifted downstream, reflecting the decayed formation of the vortex clusters owing to the installation of rear protrusions. These flow alterations contributed to the observed reductions in the peaks of the lift and sound pressure fluctuation spectra, as shown in Fig. 7 and 8, respectively. Additionally, Fig. 15 (d) shows that the pressure fluctuation around the front protrusions is small in this configuration. However, in the case shown in Fig. 15 (b), high-pressure fluctuations were induced near the top and bottom surfaces, which can be attributed to the large flow separation. Consequently, the peaks in the lift and sound pressure fluctuation spectra intensified.

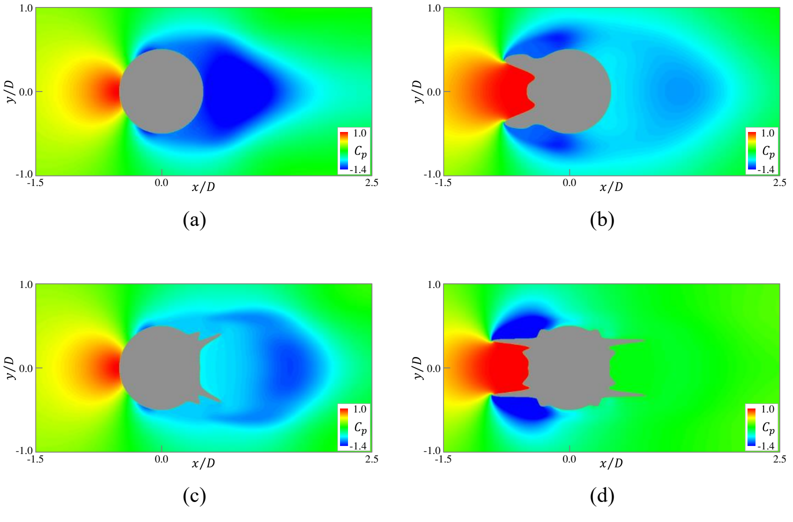

(a) (b)

(c) (d)

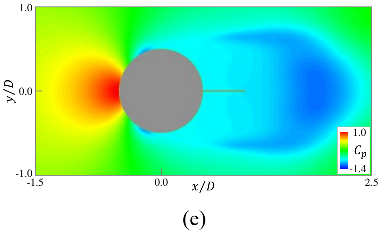

(e)

Fig. 9. Contours of the time- and spanwise-averaged pressure coefficients around the cylinder (a) without control; (b) with front protrusions; (c) with rear protrusions; (d) with front and rear protrusions; (e) with a splitter plate.

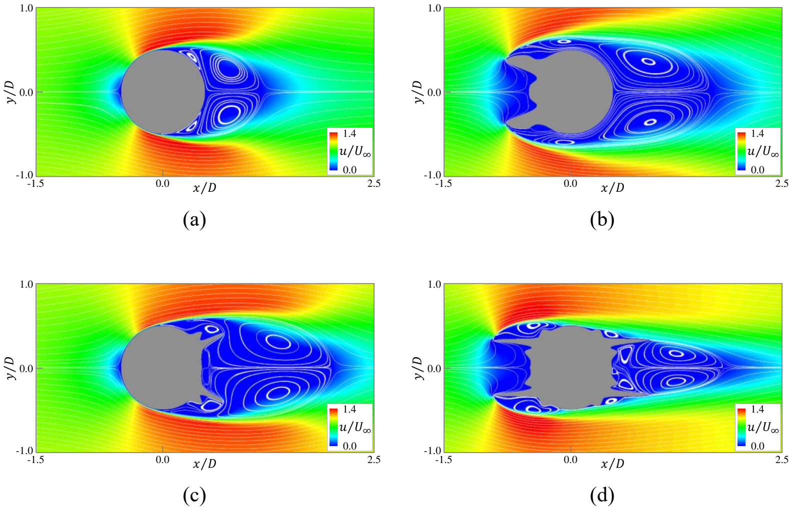

(a) (b)

(c) (d)

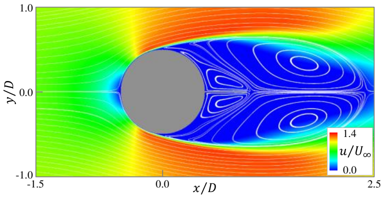

(e)

Fig. 10. Time- and spanwise-averaged streamwise velocity distributions and streamlines around the cylinder (a) without control; (b) with front protrusions; (c) with rear protrusions; (d) with front and rear protrusions; (e) with a splitter plate.

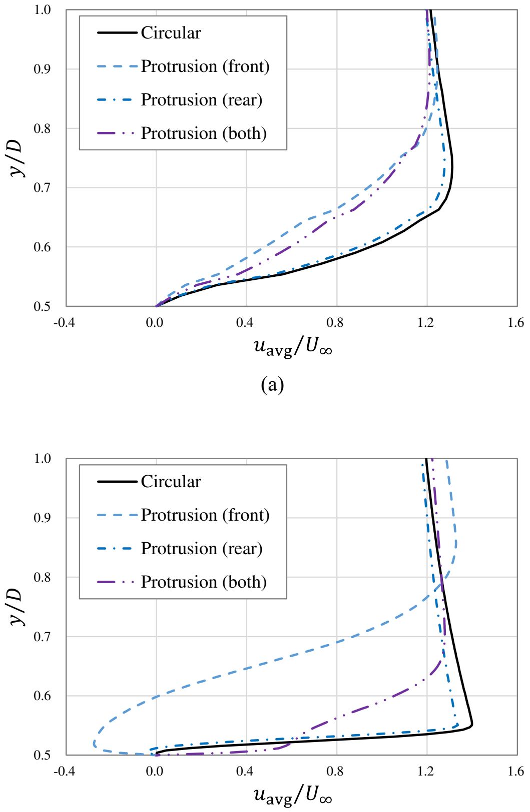

(a)

(b)

Fig. 11. Time-averaged streamwise velocity profiles at $x/D = 0.0$ at (a) $\mathrm{Re} = 150$ and (b) $\mathrm{Re} = 67000$

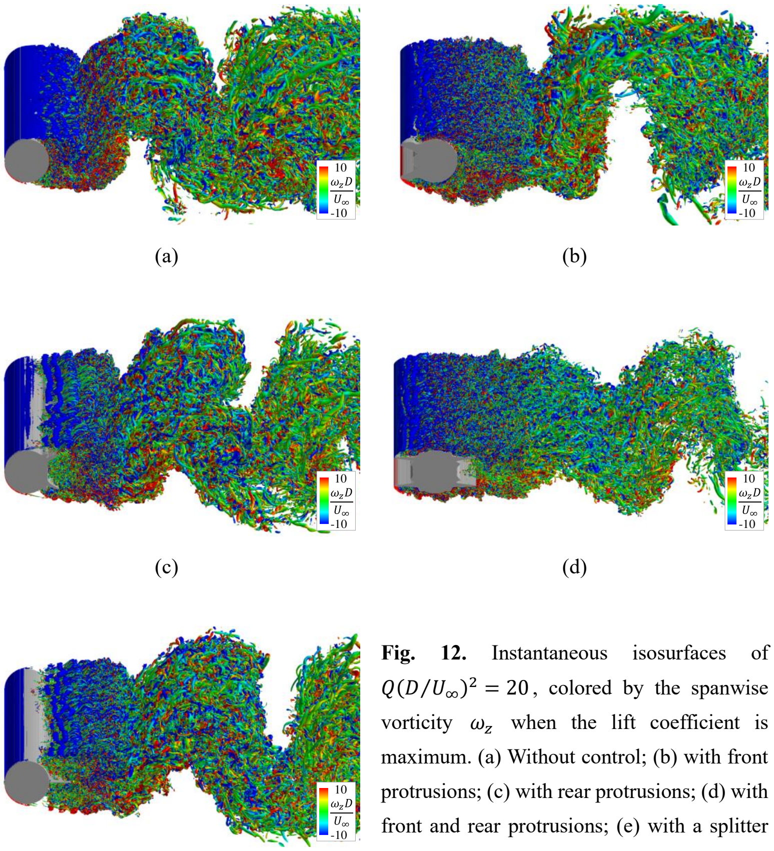

(a)

(b)

(c)

(d)

(e)

Fig. 12. Instantaneous isosurfaces of $Q(D/U_\infty)^2 = 20$, colored by the spanwise vorticity ω_z when the lift coefficient is maximum. (a) Without control; (b) with front protrusions; (c) with rear protrusions; (d) with front and rear protrusions; (e) with a splitter plate.

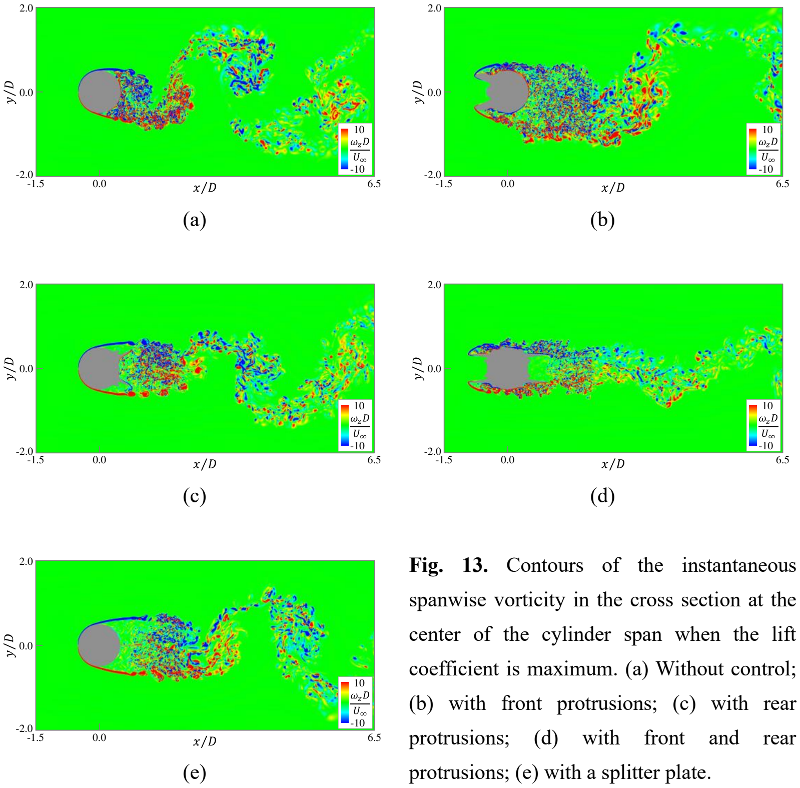

(a)

(b)

(c)

(d)

(e)

Fig. 13. Contours of the instantaneous spanwise vorticity in the cross section at the center of the cylinder span when the lift coefficient is maximum. (a) Without control; (b) with front protrusions; (c) with rear protrusions; (d) with front and rear protrusions; (e) with a splitter plate.

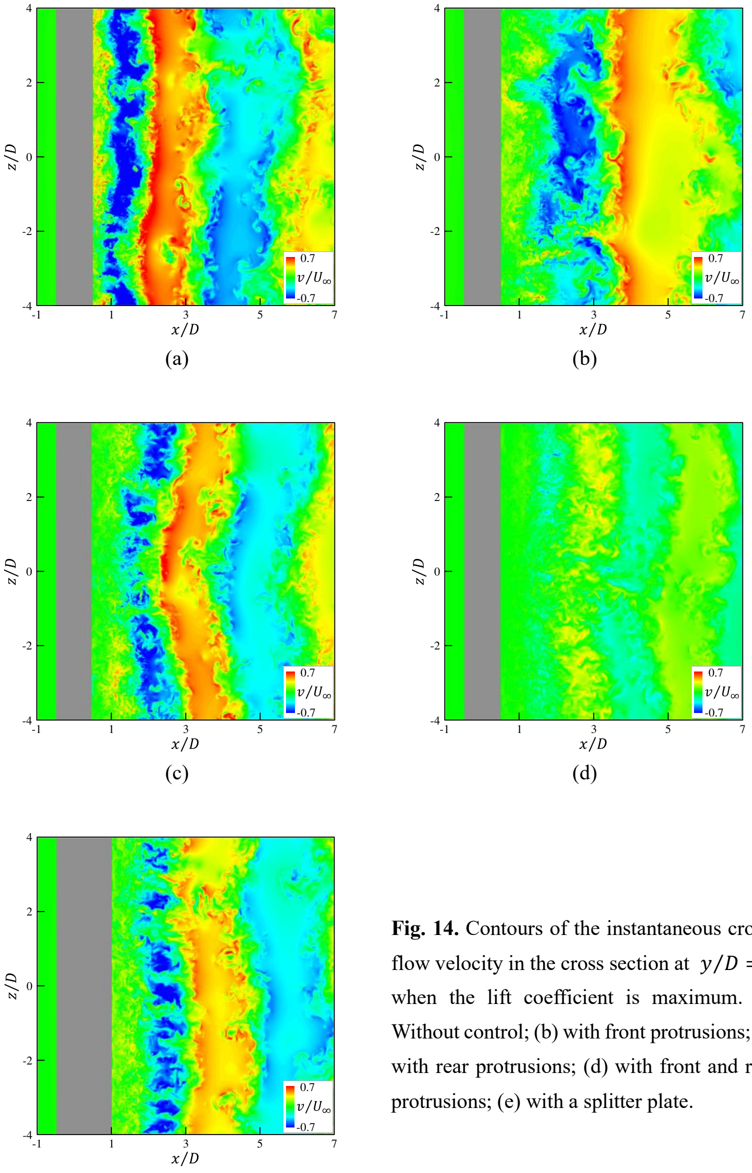

(a)

(b)

(c)

(d)

(e)

Fig. 14. Contours of the instantaneous cross-flow velocity in the cross section at $y/D = 0$ when the lift coefficient is maximum. (a) Without control; (b) with front protrusions; (c) with rear protrusions; (d) with front and rear protrusions; (e) with a splitter plate.

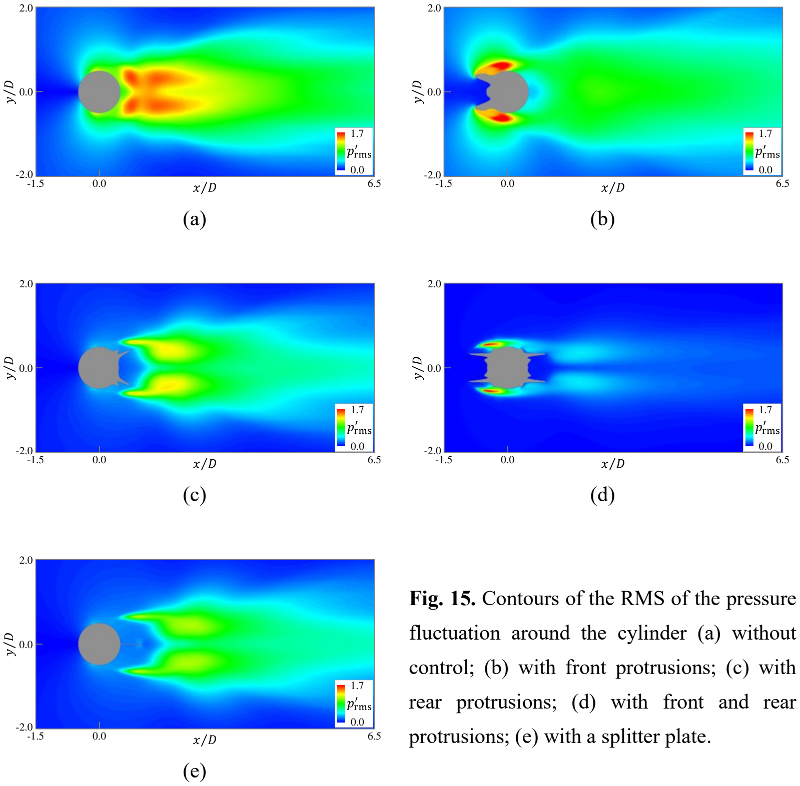

(a)

(b)

(c)

(d)

(e)

Fig. 15. Contours of the RMS of the pressure fluctuation around the cylinder (a) without control; (b) with front protrusions; (c) with rear protrusions; (d) with front and rear protrusions; (e) with a splitter plate.

4.4. **Protrusion effects on acoustic field**

In this subsection, the effects of the control methods on the acoustic field are discussed. Figure 16 shows the distributions of the instantaneous pressure fluctuations in the far field when the lift coefficient is maximum. In the uncontrolled case and the controlled case using only the front protrusions, the centers of the concentric sound waves seem to align with that of the cylinder, indicating that the lift dipoles were the predominant sound source. As shown in Fig. 16 (b), the wavelength associated with the cylinder having the front protrusions is longer than that associated with the bare circular cylinder. Moreover, the amplitudes of the waves in the front protrusion case were greater than those of the waves in the uncontrolled case. For configurations featuring rear protrusions, the centers of sound radiation shifted downstream, mirroring the delayed wake oscillation. A comparison of the acoustic fields indicates that the two configurations with rear protrusions significantly reduced the generation of aerodynamic sounds. Furthermore, the rear protrusions altered the direction of sound propagation more significantly than the splitter plate. Figure 16 (d) shows several shorter waves in addition to the primary waves. These high-frequency sounds may be contributed by turbulent flows around the protrusions. These sounds are sufficiently small compared with the primary peak sound, as shown in Fig. 8.

The directivity of the aerodynamic sound was compared with and without the application of the control methods. Figure 17 shows the RMS of the pressure fluctuations along the circumferential direction at $r/D = 64$. The uncontrolled cylinder exhibited directivity with a well -known dipole characteristic that was primarily influenced by lift fluctuations. In the cases where rear protrusions were used, the directivity patterns suggest a transition toward a more pronounced quadrupole sound, realized by the significant attenuation of the lift dipole component.

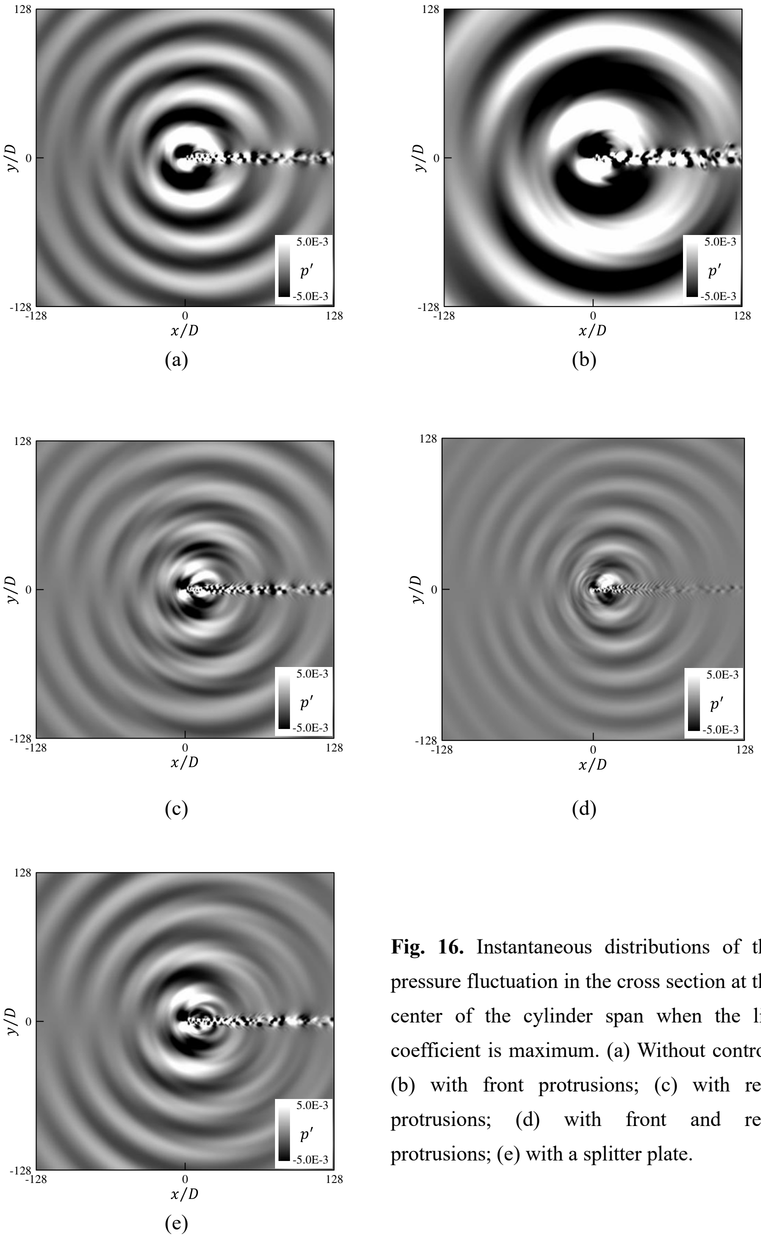

(a)

(b)

(c)

(d)

(e)

Fig. 16. Instantaneous distributions of the pressure fluctuation in the cross section at the center of the cylinder span when the lift coefficient is maximum. (a) Without control; (b) with front protrusions; (c) with rear protrusions; (d) with front and rear protrusions; (e) with a splitter plate.

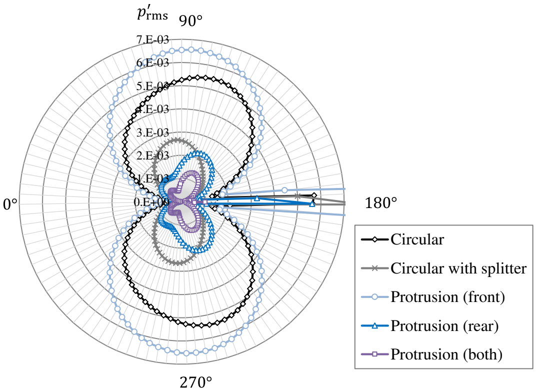

Fig. 17. Polar diagram of the RMS of the pressure fluctuation at $r/D = 64$.

5. Conclusions

Passive control methods using surface protrusions were found to be effective in reducing the aerodynamic sound generated from a cylinder. Although cylinder protrusions have been previously designed at a low Reynolds number (Re = 150) through an adjoint-based aeroacoustic shape optimization, their performance at higher Reynolds numbers, which are typically observed in mechanical engineering applications, has been unexplored. This study assessed the applicability of these protrusions at a moderate Reynolds number (Re = 67,000) using aeroacoustic simulations based on the LBM.

Three protrusion configurations were evaluated. Each configuration can reduce the mean drag by at least 45% compared with the unmodified circular cylinder. Two configurations with rear protrusions can surpass the sound attenuation performance of the conventional splitter plate. The application of symmetric protrusions on both the front and rear surfaces notably reduced the tonal sound by 13 dB. These results suggest that rear protrusions can effectively suppress wake oscillations and dipole sound generation, particularly in the subcritical range of the Reynolds number. In contrast, a specific front protrusion led to an increase in the low-frequency sound due to large-scale flow separation induced by the front protrusions. These findings highlight the need to tailor the front protrusion shape to the Reynolds number of the flow for performance optimization.

Because of the substantial pressure difference between the inside and outside of the front protrusions, the material strength and applicable flow velocity should be carefully considered. Another limitation of protrusions is its dependency on the flow direction. This constraint may be alleviated by optimization considering multiple flow directions.

6. Acknowledgment

This study was supported by the JSPS KAKENHI (Grant Number JP22K03929). Computational resources were provided by the Research Institute for Information Technology at Kyushu University.

References

[1] H.D. Yao and L. Davidson, Phys. Fluids **30**, (2018).

[2] K.K. Chode, H. Viswanathan, and K. Chow, Phys. Fluids **33**, (2021).

[3] K.K. Chode, H. Viswanathan, K. Chow, and H. Reese, Phys. Fluids **35**, (2023).

[4] H. Li, X. Liu, D. Thompson, and G. Squicciarini, Appl. Acoust. **188**, 108542 (2022).

[5] L. Qi-liang, L. Zhuo-ming, O. Meng-han, and Y. Zhi-gang, Appl. Acoust. **193**, 108777 (2022).

[6] T. Li, D. Qin, N. Zhou, J. Zhang, and W. Zhang, Appl. Acoust. **196**, 108886 (2022).

[7] T.R. Ricciardi, W.R. Wolf, N.J. Moffitt, J.R. Kreitzman, and P. Bent, J. Sound Vib. **496**, 115933 (2021).

[8] V. Kopiev, I. Belyaev, M. Zaytsev, and K. Zhao, J. Sound Vib. **511**, 116362 (2021).

[9] Y. Zhang, B. Chen, K. Zhao, X. Tang, X. Yang, and G. Hu, Phys. Fluids **35**, (2023).

[10] H. Choi, W.P. Jeon, and J. Kim, Annu. Rev. Fluid Mech. **40**, 113 (2008).

[11] W.L. Chen, Y. Huang, C. Chen, H. Yu, and D. Gao, Ocean Eng. **258**, 111840 (2022).

[12] M. Zhao, Ocean Eng. **285**, 115389 (2023).

[13] S. Karimi, B. Mohammadikalakoo, and P. Schito, J. Wind Eng. Ind. Aerodyn. **209**, 104488 (2021).

[14] Z. Chen and C.Y. Wen, J. Fluids Struct. **103**, 103292 (2021).

[15] G. Minelli, T. Dong, B.R. Noack, and S. Krajnović, J. Fluid Mech. **893**, (2020).

[16] Z.X. Qiao, G. Minelli, B.R. Noack, S. Krajnović, and V. Chernoray, J. Wind Eng. Ind. Aerodyn. **212**, (2021).

[17] C. Zheng, T. Ji, F. Xie, X. Zhang, H. Zheng, and Y. Zheng, Phys. Fluids **33**, (2021).

[18] F. Ren, C. Wang, and H. Tang, Phys. Fluids **33**, (2021).

[19] E. Amico, G. Cafiero, and G. Iuso, Phys. Fluids **34**, (2022).

[20] D. You, H. Choi, M.R. Choi, and S.H. Kang, AIAA J. **36**, 1961 (1998).

[21] F. Duan and J. Wang, J. Fluid Mech. **920**, (2021).

[22] B. Mahato, N. Ganta, and Y.G. Bhumkar, J. Sound Vib. **494**, 115906 (2021).

[23] F. Eydi and A. Mojra, (2023).

[24] T.F. Geyer, Appl. Acoust. **195**, 108834 (2022).

[25] H. Du, Q. Zhang, Q. Li, W. Kong, and L. Yang, Phys. Fluids **34**, (2022).

[26] H.S. Yoon, K.J. Oh, H.J. Kim, M. Il Kim, and J. Moon, Ocean Eng. **195**, 106713 (2020).

[27] H. Bai, Z. Lu, R. Wei, Y. Yang, and Y. Liu, Phys. Fluids **33**, (2021).

[28] K. Kusano, Comput. Fluids **248**, 105662 (2022).

[29] K. Kusano, Phys. Fluids **35**, (2023).

[30] S. Moreau, Phys. Fluids **34**, (2022).

[31] M. Geier, A. Greiner, and J.G. Korvink, Phys. Rev. E - Stat. Nonlinear, Soft Matter Phys. **73**, 1 (2006).

[32] L. Fei, K.H. Luo, and Q. Li, Phys. Rev. E **97**, 53309 (2018).

[33] F. Nicoud and F. Ducros, Flow, Turbul. Combust. **62**, 183 (1999).

[34] M. Weickert, G. Teike, O. Schmidt, and M. Sommerfeld, Comput. Math. with Appl. **59**, 2200 (2010).

[35] C. Norberg, J. Fluids Struct. **17**, 57 (2003).

[36] K. Nakahashi and L.S. Kim, AIAA Pap. 676 (2004).

[37] D. V. Gaitonde and M.R. Visbal, AIAA J. **38**, 2103 (2000).

[38] E.W.S. Kam, R.M.C. So, and R.C.K. Leung, AIAA J. **45**, 1703 (2007).

[39] D. Yu, R. Mei, and W. Shyy, 41st Aerosp. Sci. Meet. Exhib. **8**, 953 (2003).

[40] J.H. Seo and Y.J. Moon, J. Sound Vib. **306**, 564 (2007).

[41] T.P. Lloyd and M. James, Appl. Ocean Res. **59**, 676 (2016).

[42] F. Lesage and I.S. Gartshore, J. Wind Eng. Ind. Aerodyn. **25**, 229 (1987).

[43] C. Zheng, P. Zhou, S. Zhong, X. Zhang, X. Huang, and R.C.H. So, Phys. Fluids **33**, (2021).

[44] H. Nishimura and Y. Taniike, J. Wind Eng. Ind. Aerodyn. **89**, 713 (2001).

[45] Y. Xing, P. Liu, H. Guo, and L. Li, Appl. Acoust. **122**, 152 (2017).

[46] K. Kusano, K. Yamada, and M. Furukawa, J. Sound Vib. **467**, 115044 (2020).

[47] T.F. Geyer, Exp. Fluids **61**, 1 (2020).